Supplementary Information

Construction of CoP/Co_2P Heterojunctions on Hollow Carbon Rods as Efficient Bifunctional Electrocatalysts for Overall Water Splitting

Table of Contents

Supplementary Notes

Chemicals and materials

All reagents without further purification prior to use. Ultrapure water (18.2 MΩ·cm) was used throughout all the experiments. Ligand 5,5'-(5-(1H-imidazol-1-yl)-1,3-phenylene)bis(1H-tetrazole) (H_2IPBT, 97%) was obtained from the Shanghai Kaiyulin Pharmaceutical Technology Co., Ltd. Cobalt chloride hexahydrate ($CoCl_2·6H_2O$, AR), Sodium hypophosphite monohydrate ($NaH_2PO_2·H_2O$, 99%), N, N-Dimethylacetamide (DMAc, 99.0%), isopropanol (IPA, GC, ≥99.9%) and Potassium hydroxide (KOH, 99.99 %) were commercially available from Shanghai Aladdin Biochemical Technology Co., Ltd. Nafion® perfluorinated resin solution (5 wt. % in mixture of lower aliphatic alcohols and water, contains 45% water) was sourced from Sigma-Aldrich. Acetone was purchased from Sinopharm Chemical Reagent Co., Ltd. Pt/C catalyst (TKK-20, 20 wt%) was obtained from TANAKA. Ruthenium (IV) oxide (RuO_2, 99.9% metals basis) was purchased from Macklin Biochemical Co., Ltd. The anion exchange membrane (AEM, X37-50 grade T membrane) and Carbon paper were purchased from Suzhou Sinero Technology Co., Ltd.

Characterizations

The crystallinity and phase purity of the as-synthesized materials were characterized by powder X-ray diffraction (PXRD) on a Bruker D8 diffractometer (Bruker AXS, Karlsruhe, Germany) using Cu-Kα radiation (λ = 1.5406 Å). The surface morphologies of the samples were examined using a Nova NanoSEM 230 scanning electron microscope (FEI Czech Republic S.R.O.). High-resolution transmission electron microscopy (HRTEM) images were acquired with a FEI TECNAI G2 F20 field emission transmission electron microscope at an operating voltage of 200 kV. Raman spectra were acquired using a WITec Alpha 300R confocal Raman microscope (Germany) with a 532 nm excitation laser. N_2 adsorption-desorption isotherms were measured at 77 K using a Micromeritics ASAP 2460 analyzer to characterize the pore structure of the catalysts. X-ray photoelectron spectroscopy (XPS)

measurements were conducted using a ThermoFisher-VG Scientific photoelectron spectrometer (K-Alpha^{+}), with all binding energies calibrated against the C 1s peak at 284.8 eV.

Calibration of the reference electrode

Prior to electrochemical measurements, the Hg/HgO reference electrode was calibrated against the reversible hydrogen electrode (RHE) in high-purity hydrogen-saturated 1.0 M KOH electrolyte at 25 °C. The calibration was conducted using a Pt foil as both the working and counter electrode, and the Hg/HgO reference electrode was used as the reference electrode. Cyclic voltammetry was run at a scan rate of 1 mV·s^{-1}, and the potential at which the current crossed zero was designated as the RHE potential (vs. Hg/HgO). The results are shown in **Figure S1**, where E(RHE) = E(Hg/HgO) + 0.924 V.

Supplementary electrochemical measurements

The double-layer capacitance (C_{dl}) was determined from CV measurements in a non-Faradaic potential window. CV curves were recorded at different scan rates (20, 40, 60, 80, 100 mV·s^{-1}), and the capacitive current density at a specific potential was plotted versus the scan rate. The slope of the linear regression gives the C_{dl} (mF·cm^{-2}), which is then used to estimate the electrochemical active surface area (ECSA) according to the Equation S2.

$$C_{dl} = \Delta J/2\upsilon = (J_a - J_c)/2\upsilon \quad \text{(Equation S1)}$$

$$ECSA = C_{dl}/C_s \quad \text{(Equation S2)}$$

In Equations S1 and S2, ΔJ denotes the difference between the anodic (J_a) and cathodic (J_c) current densities (mA·cm^{-2}), υ is the scan rate (V·s^{-1}), and C_s is a constant representing the specific double-layer capacitance of an ideal smooth electrode surface. A direct proportionality exists between the ECSA and C_{dl}, meaning that an increase in C_{dl} corresponds to a larger ECSA, which signifies a higher density of exposed active sites and enhanced electrocatalytic activity.

Faraday Efficiency (FE) measurement experiment

The Faradaic Efficiency was evaluated using a water displacement method in an H-type electrolyzer. Under standard ambient temperature and pressure (SATP) conditions (25 °C, 1 atm) and at a fixed current of 50 mA, the hydrogen and oxygen produced were collected separately in 50 mL graduated glass tubes. Their volumes were recorded periodically. The accumulated charge transferred through the working electrode was determined using the formula:

$$Q = It \qquad \text{(Equation S3)}$$

where Q is the total theoretical electric charge, I is the current in ampere (A), and t is the time in seconds (s).

The FE was calculated by the following equations:

$$FE = \frac{n*F*V}{Q*V_m} \times 100\% \qquad \text{(Equation S4)}$$

where n is 2 for HER and 4 for OER, respectively, F is the Faraday constant (96485 $A \cdot s \cdot mol^{-1}$), V is the gas (hydrogen or oxygen) volume measured by the drainage method at a current of 50 mA under the SATP conditions (25 ± 1 °C), and V_m is the molar volume (24.465 $L \cdot mol^{-1}$, SATP).

Density functional theory (DFT) computational

All DFT calculations were performed utilizing the Vienna Ab-initio Simulation Package (VASP) as the foundational framework. The Perdew-Burke-Ernzerhof (PBE) functional, employed within the framework of the generalized gradient approximation (GGA) method, has been utilized to elucidate the exchange-correlation effects [1]. The core-valence interactions were estimated via the projected augmented wave (PAW) method. A plane-wave energy cutoff of 450 eV and a *k*-point grid of 5×5×1 generated by the Monkhorst-Pack scheme were adopted for Brillouin zone sampling. To avoid periodic interactions, a vacuum space of 15 Å above the surfaces is adopted. Structural optimizations were considered converged when the energy and force thresholds reached 1.0×10^{-5} eV and 0.02 $eV \cdot Å^{-1}$, respectively. Visual modeling of crystal structures and visualization of volumetric data were performed using VESTA software [2].

The adsorption energy (E_{ads}) was calculated as:

$$E_{ads} = E(A+B) – E(A) – E (B) \quad \text{(Equation S5)}$$

where E(A+B) is the calculated energy of adsorption configuration, and E(A) and E(B) are the calculated energy of the substrate and the adsorbate in their isolated states, respectively.

The Gibbs free energy change (ΔG) for each reaction step was evaluated using:

$$\Delta G = \Delta E + \Delta E_{ZPE} - T\Delta S \quad \text{(Equation S6)}$$

where ΔE is the electronic energy difference directly obtained from DFT calculations, ΔE_{ZPE} is the zero-point energy difference, T is the room temperature (298.15 K) and ΔS is the entropy change.

Supplementary Figures

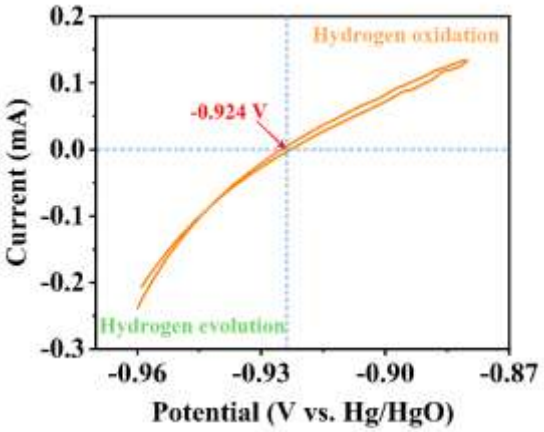

Figure S1. Reversible hydrogen electrode (RHE) test in a hydrogen-saturated 1.0 M KOH solution at 25 °C. Reversible hydrogen electrode (RHE) test in a hydrogen-saturated 1.0 M KOH solution at 25 °C.

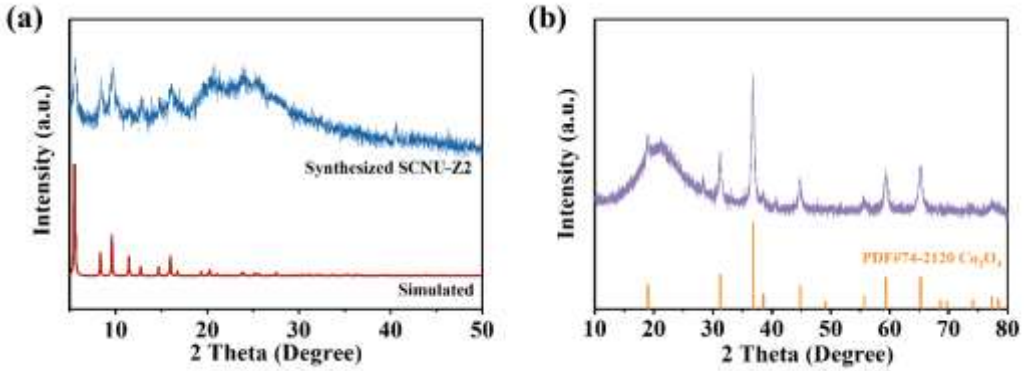

Figure S2. (a) The PXRD pattern of the SNCU-Z2 MOF. (b) The PXRD pattern of Co_3O_4@NC.

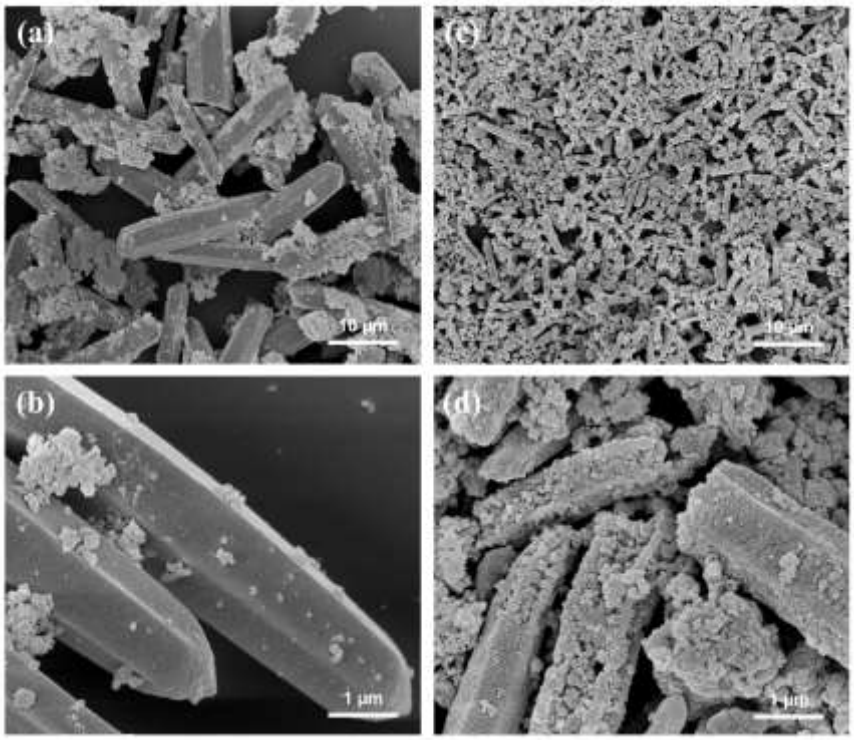

Figure S3. (a) SEM images of (a-b) SCNU-Z2 and (c-d) Co_3O_4@NC at different magnifications.

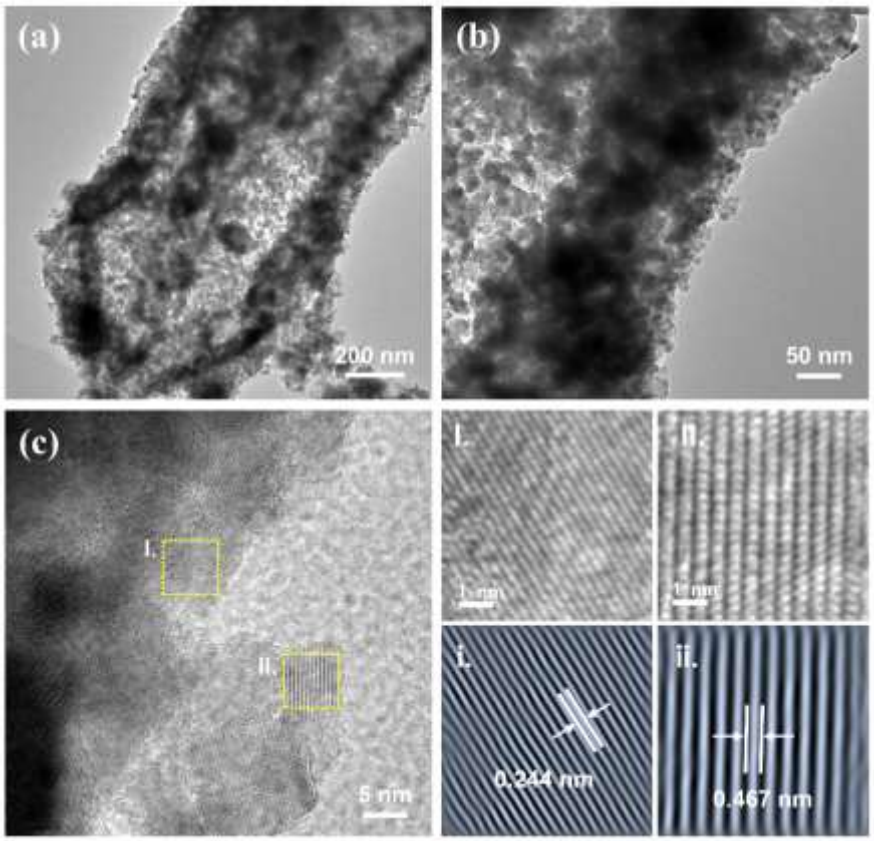

Figure S4. TEM images of Co_3O_4@NC at different magnifications; (c) HRTEM image of Co_3O_4@NC and local enlarged areas (I and II) and their corresponding IFFT images.

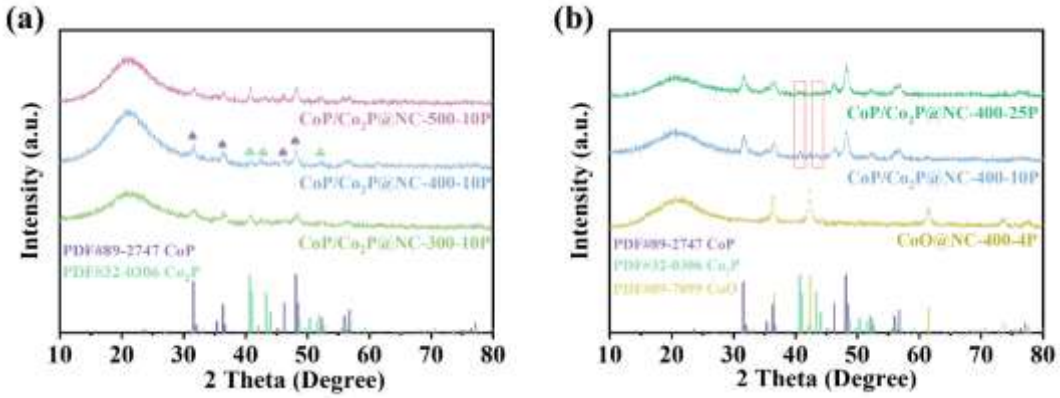

Figure S5. (a) The PXRD patterns of CoP/Co_2P@NC-300-10P, CoP/Co_2P@NC-400-10P and CoP/Co_2P@NC-500-10P. (b) The PXRD patterns of CoO@NC-400-4P, CoP/Co_2P@NC-400-10P and CoP/Co_2P@NC-400-25P.

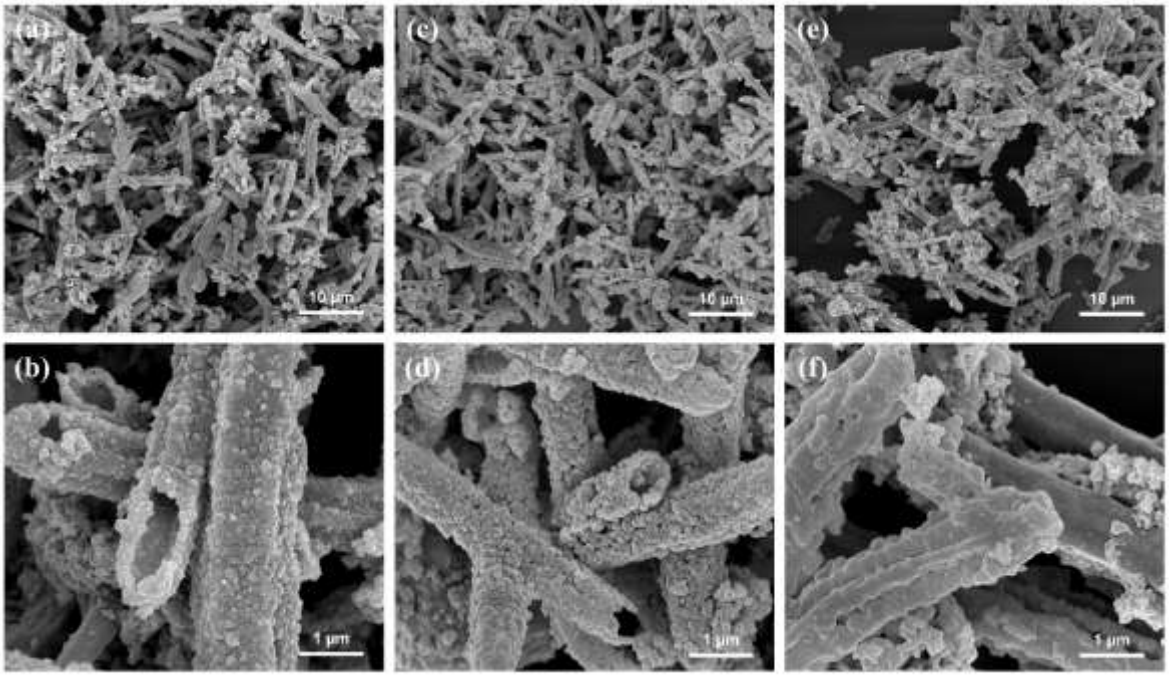

Figure S6. SEM images of (a-b) CoP/Co_2P@NC-400-10P, (c-d) CoP/Co_2P@NC-300-10P and (e-f) CoP/Co_2P@NC-500-10P at different magnifications.

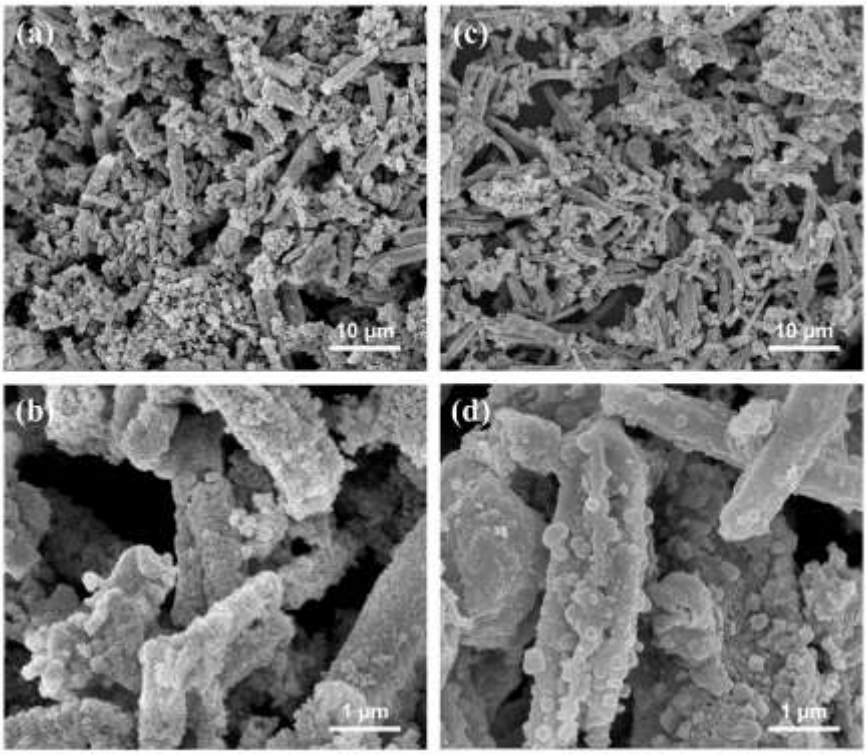

Figure S7. SEM images of (a-b) CoO@NC-400-4P and (c-d) CoP/Co_2P@NC-400-25P at different magnifications.

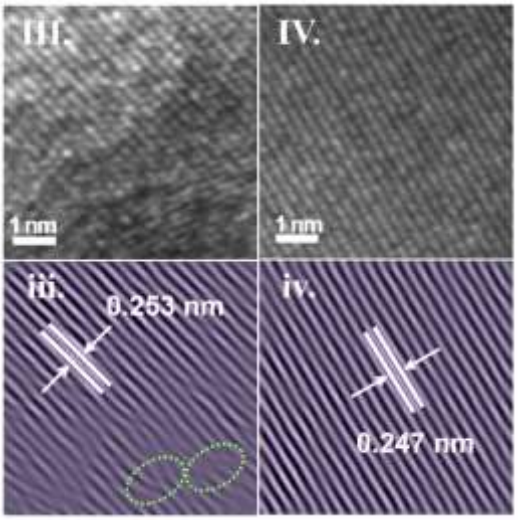

Figure S8. Local magnified areas (III-IV) of CoP/Co_2P@NC-400-10P in **Figure 1e** and its corresponding IFFT images (iii-iv).

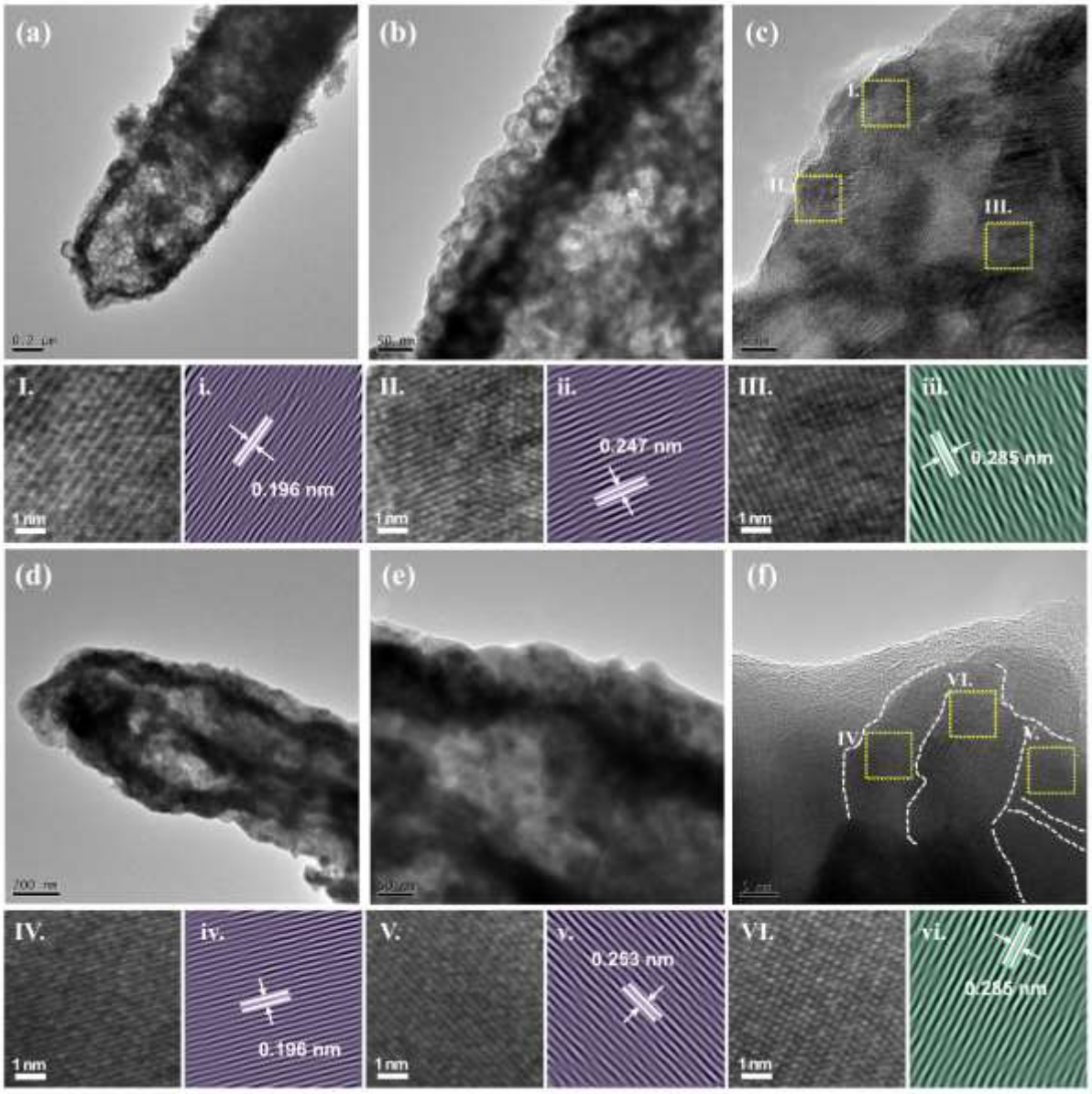

Figure S9. (a-c) TEM images of CoP/Co_2P@NC-300-10P at different magnifications. (c) HRTEM image and local magnified areas (I-III) and corresponding IFFT images (i-iii) of CoP/Co_2P@NC-300-10P. (d-e) TEM images of CoP/Co_2P@NC-500-10P at different magnifications; (f) HRTEM image and local magnified areas (IV-VI) and the corresponding IFFT images (iv-vi) of CoP/Co_2P@NC-500-10P.

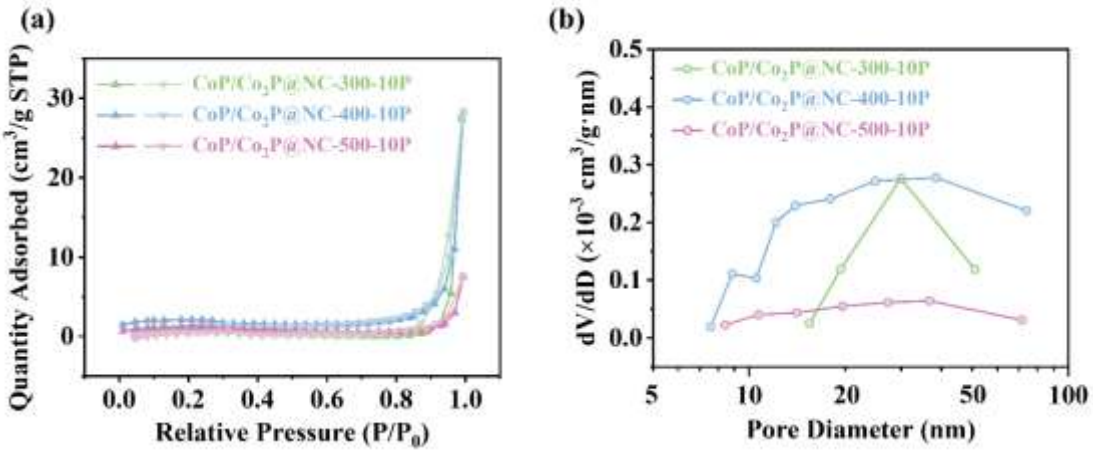

Figure S10. (a) N_2 adsorption/desorption isotherms of CoP/Co_2P@NC-300-10P, CoP/Co_2P@NC-400-10P and CoP/Co_2P@NC-500-10P at 77K. (b) Pore size distribution plot by BJH method analysis of CoP/Co_2P@NC-300-10P, CoP/Co_2P@NC-400-10P and CoP/Co_2P@NC-500-10P catalysts.

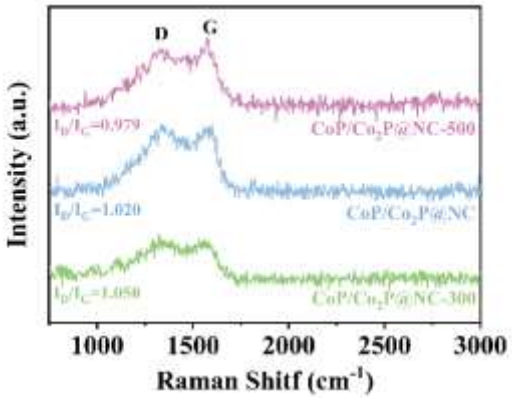

Figure S11. Raman spectra of CoP/Co_2P@NC-300-10P, CoP/Co_2P@NC-400-10P and CoP/Co_2P@NC-500-10P.

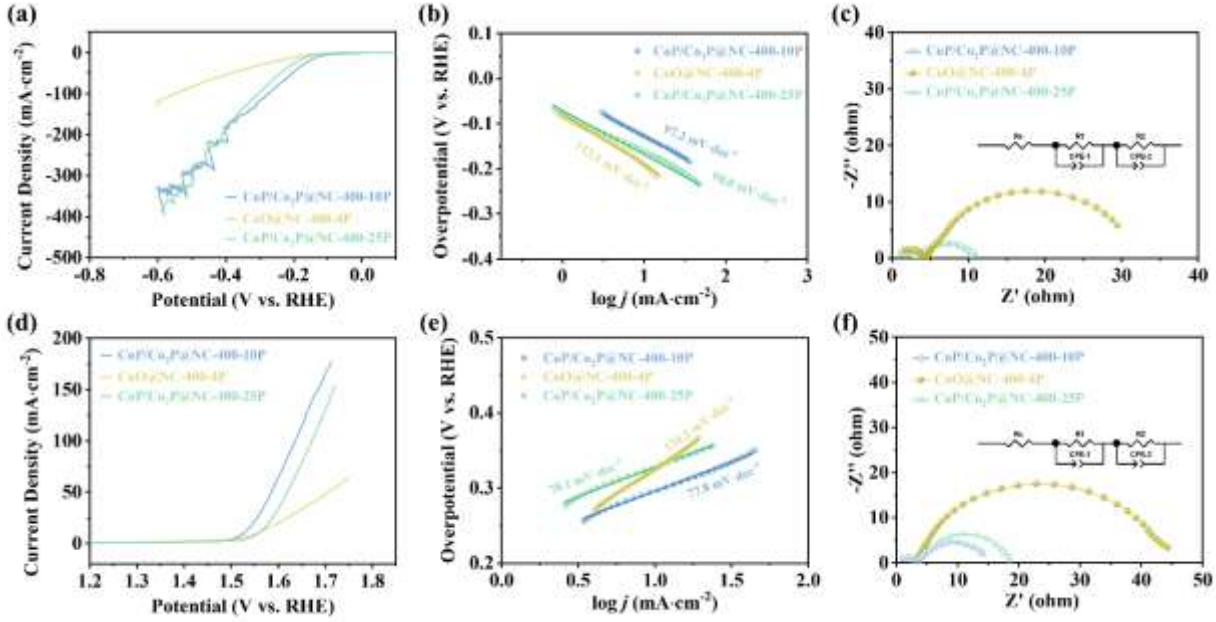

Figure S12. (a) HER polarization curves of electrocatalysts CoP/Co_2P@NC-400-10P, CoO@NC-400-4P and CoP/Co_2P@NC-400-25P measured in 1.0 M KOH solution with iR compensation. (b) Corresponding Tafel plots for the HER on CoP/Co_2P@NC-400-10P and reference catalysts. (c) Nyquist plots of various catalysts with frequency from 0.01 to 10^5 Hz at -1.15 V vs. Hg/HgO. (d) OER polarization curves of electrocatalysts CoP/Co_2P@NC-400-10P, CoO@NC-400-4P and CoP/Co_2P@NC-400-25P measured in 1.0 M KOH solution with 90% iR compensation. (e) Corresponding Tafel plots for the OER on CoP/Co_2P@NC-400-10P and reference catalysts. (f) Nyquist plots of various catalysts with frequency from 0.01 to 10^5 Hz at 0.605 V vs. Hg/HgO.

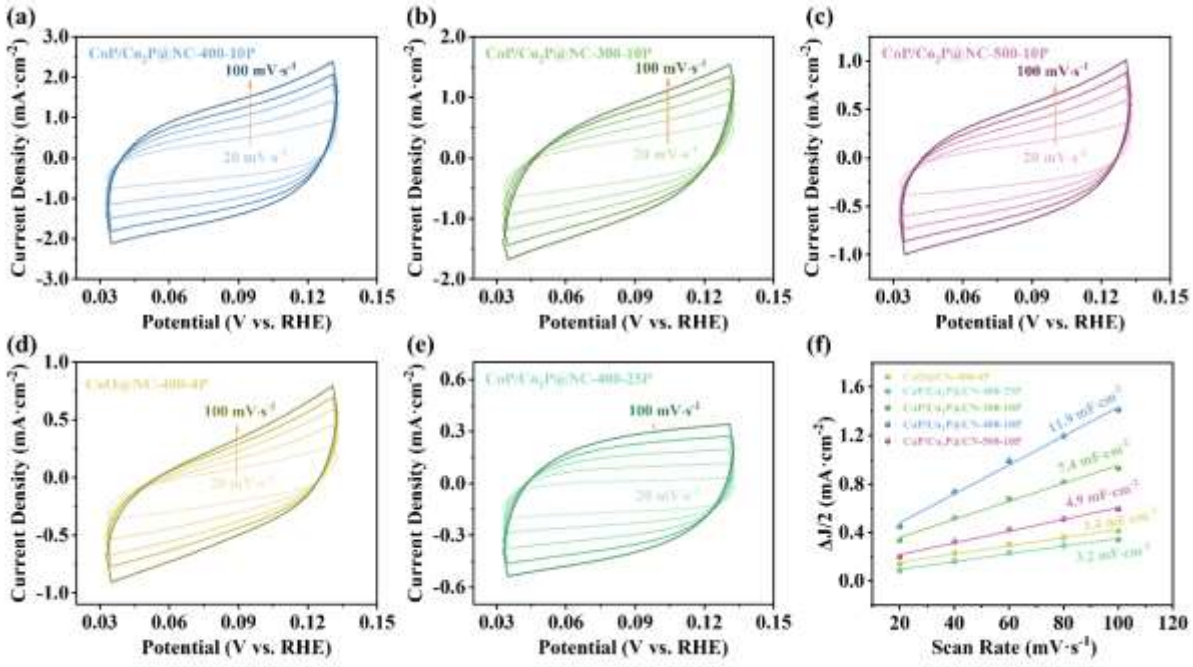

Figure S13. Cyclic voltammograms of (a) CoP/Co_2P@NC-400-10P, (b) CoP/Co_2P@NC-300-10P, (c) CoP/Co_2P@NC-500-10P, (d) CoO@NC-400-4P and (e) CoP/Co_2P@NC-400-25P in the non-Faradaic potential range at scan rates of 20, 40, 60, 80 and 100 $mV \cdot s^{-1}$. (f) The corresponding C_{dl} values of each catalyst.

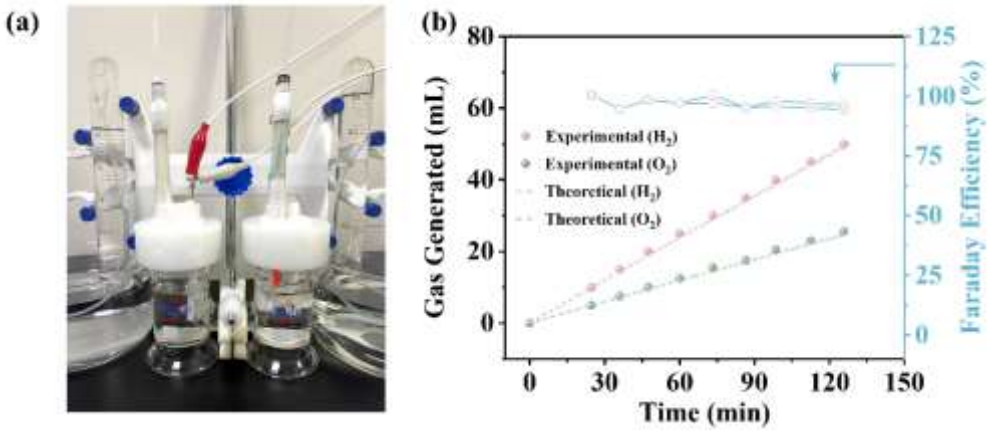

Figure S14. (a) Gas collection device of water splitting with CoP/Co_2P@NC-400-10P as both the anode and cathode in 1.0 M KOH aqueous solution. (b) Faraday efficiency of CoP/Co_2P@NC-400-10P catalyzed water electrolysis measured at the current density of 50 $mA \cdot cm^{-2}$.

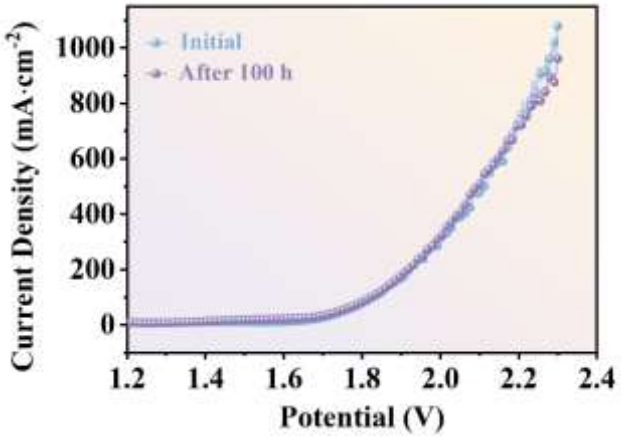

Figure S15. Polarization curves of CoP/Co_2P@NC-400-10P||CoP/Co_2P@NC-400-10P electrolyzer without iR compensation, measured initially and after 100 hours of operation.

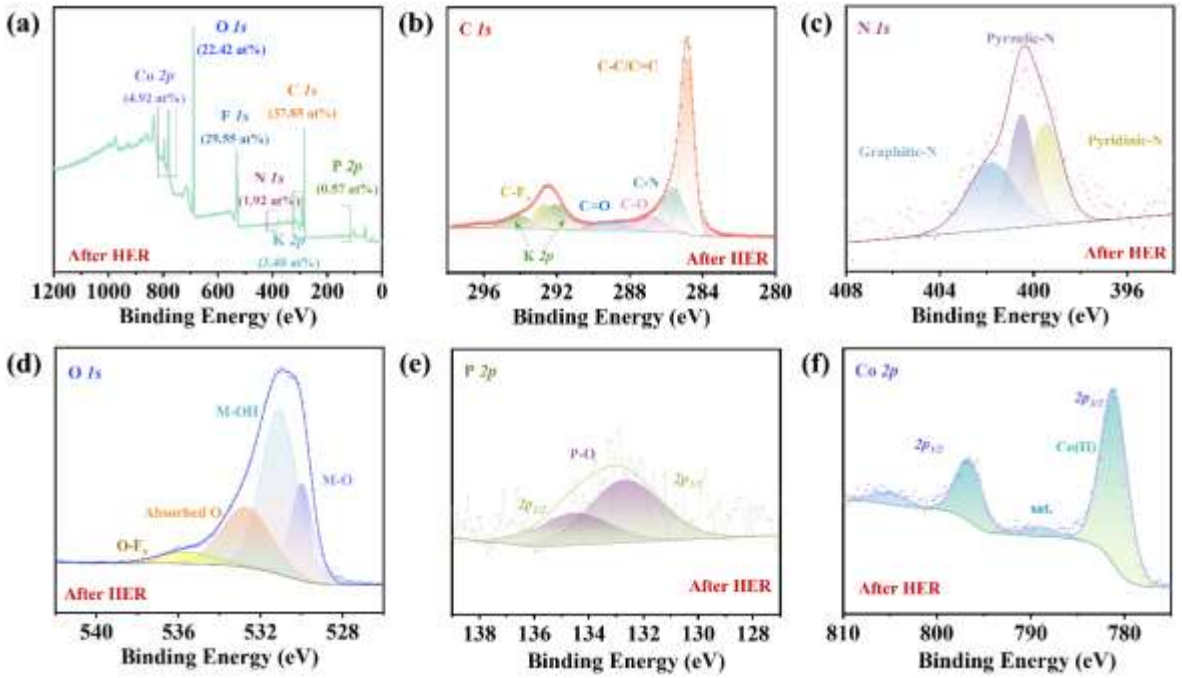

Figure S16. XPS characterization of catalyst CoP/Co_2P@NC-400-10P following 100 hours of AEM electrolyzer operation, sampled from the cathode (HER): (a) Survey spectra, (b) C 1s, (c) N 1s, (d) O 1s, (e) P 2p and (f) Co 2p high-resolution spectra.

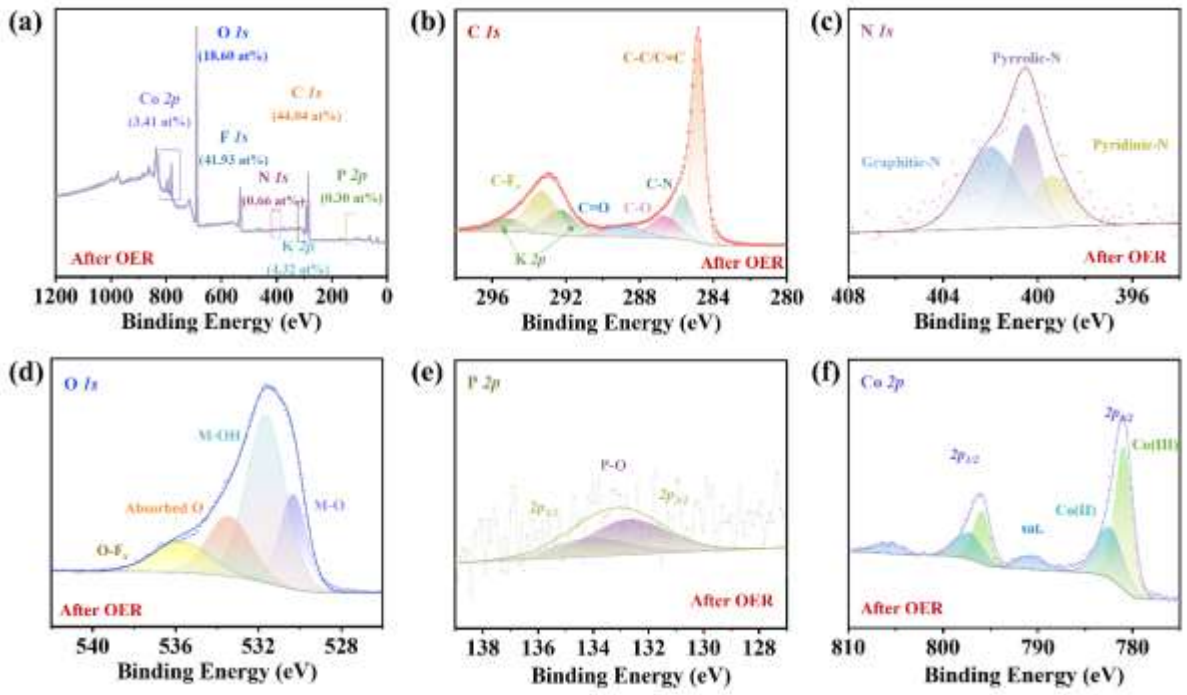

Figure S17. XPS characterization of catalyst CoP/Co_2P@NC-400-10P following 100 hours of AEM electrolyzer operation, sampled from the anode (OER): (a) Survey spectra, (b) C 1s, (c) N 1s, (d) O 1s, (e) P 2p and (f) Co 2p high-resolution spectra.

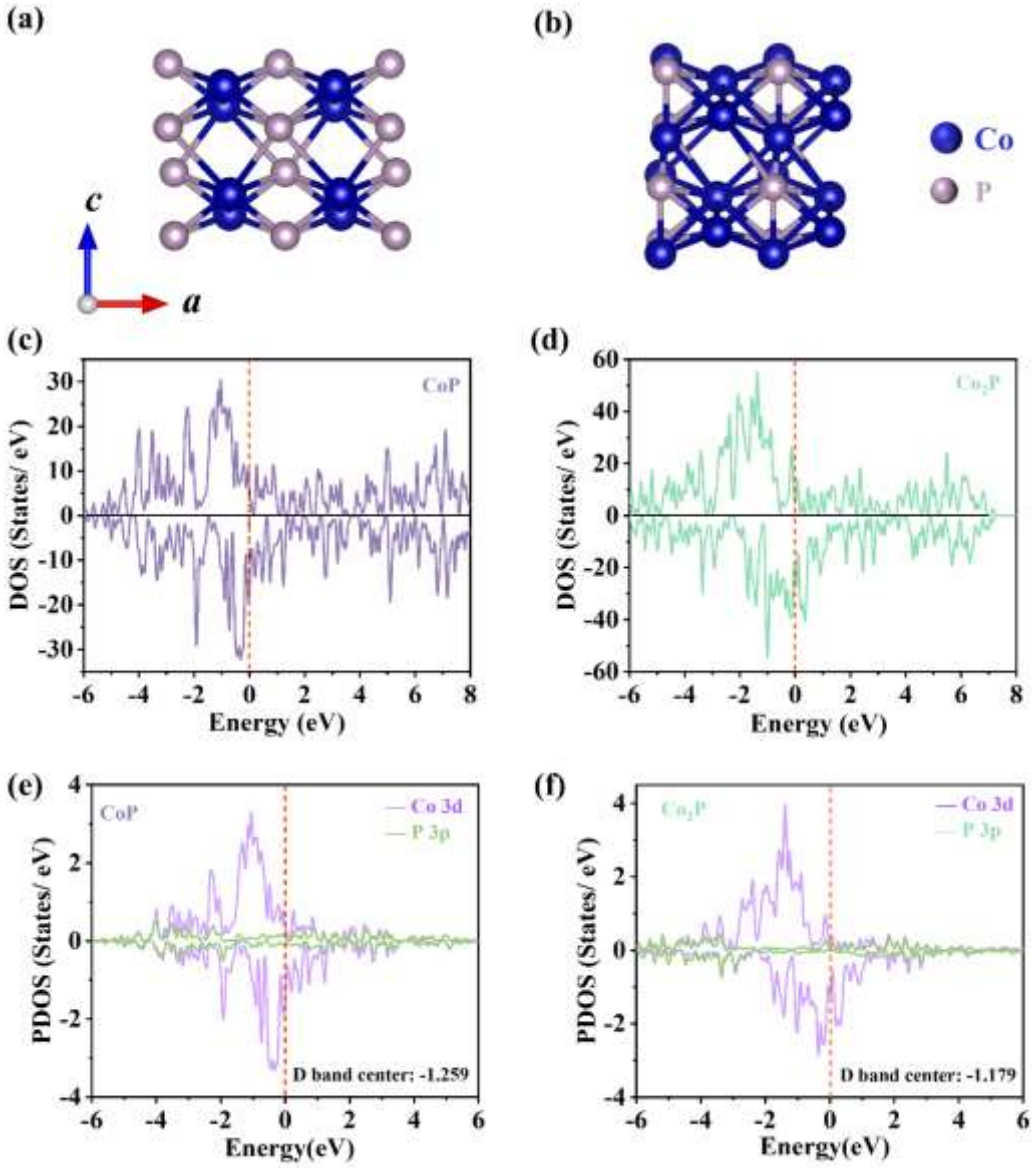

Figure S18. Structure representations of (a) CoP and (b) Co_2P. DOS for up and down spins of (c) CoP and (d) Co_2P. PDOS of Co 3d and P 3p orbitals and the corresponding d-band centers for (e) CoP and (f) Co_2P.

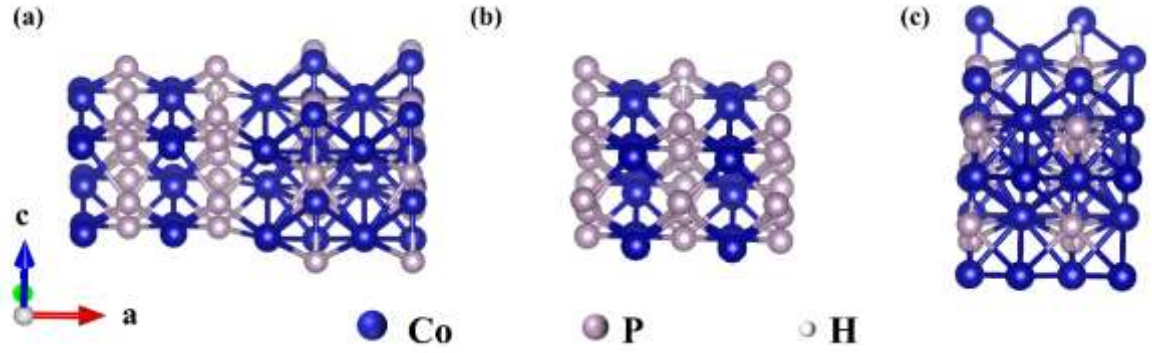

Figure S19. Schematic diagrams of H* adsorption on (a) CoP/Co_2P, (b) CoP, and (c) Co_2P.

Supplementary tables

Table S1. Summary of BET surface area and average pore diameter analysis of the as-synthesized electrocatalysts.

Catalysts	BET Surface Area(m^2/g)	Average pore diameter (4V/A by BET) (nm)	BJH method average pore diameter (nm)
CoP/Co_2P@NC-300-10P	2.63	4.39	44.98
CoP/Co_2P@NC-400-10P	5.42	6.88	46.22
CoP/Co_2P@NC-500-10P	3.18	3.26	27.01

Table S2. Comparison of η_{10} overpotentials and η_{100} of various catalysts to catalyze HER and OER.

Catalysts	HER		OER	
	η_{10} (mV)	η_{100} (mV)	η_{10} (mV)	η_{100} (mV)
CoP/Co_2P@NC-400-10P	127.6	272.3	297.4	407.1
CoP/Co_2P@NC-300-10P	180.6	338.2	319.2	420.8
CoP/Co_2P@NC-500-10P	150.5	296.4	310.9	425.3
CoO@NC-400-4P	191.4	552.2	323.8	N/A
CoP/Co_2P@NC-400-25P	160.6	305.3	327.0	441.7
Pt/C (TKK-20)	27.4	303.3	N/A	N/A
RuO_2	N/A	N/A	268.3	494.0
CP	539.6	797.0	N/A	N/A

Table S3. Fitted values of EIS Nyquist plot by the equivalent circuit model shown in Figures 3c and S11c.

Catalysts	R_s (ohm)	R_1 (ohm)	CPE_1-T (F)	CPE_1-P	R_2 (ohm)	CPE_2-T (F)	CPE_2-P	Chi-squares
CoP/Co_2P@NC-400-10P	0.40	2.79	2.00×10^{-5}	0.78	7.48	0.0200	0.76	2.40×10^{-3}
CoP/Co_2P@NC-300-10P	0.44	2.50	2.85×10^{-5}	0.85	12.12	0.0241	0.82	4.40×10^{-3}
CoP/Co_2P@NC-500-10P	0.48	3.39	2.44×10^{-5}	0.76	12.07	0.0584	0.82	3.46×10^{-3}
CoO@NC-400-4P	0.32	4.65	2.41×10^{-5}	0.75	29.23	0.0895	0.87	5.22×10^{-3}
CoP/Co_2P@NC-400-25P	0.51	3.03	6.86×10^{-6}	0.85	7.64	0.0604	0.76	4.03×10^{-3}
Pt/C (TKK-20)	0.46	4.01	3.03×10^{-5}	0.75	4.81	0.0238	0.72	3.06×10^{-3}

Table S4. Fitted values of EIS Nyquist plots by the equivalent circuit model shown in Figures 3f and S11f.

Catalysts	R_s (ohm)	R_1 (ohm)	CPE_1-T (F)	CPE_1-P	R_2 (ohm)	CPE_2-T (F)	CPE_2-P	Chi-squares
CoP/Co_2P@NC-400-10P	0.34	3.12	1.71×10^{-5}	0.77	12.05	0.0545	0.80	5.14×10^{-3}
CoP/Co_2P@NC-300-10P	0.41	3.93	5.55×10^{-6}	0.84	30.26	0.0409	0.82	4.19×10^{-3}
CoP/Co_2P@NC-500-10P	0.42	2.80	1.33×10^{-5}	0.80	17.15	0.0531	0.85	4.79×10^{-3}
CoP/Co_2P@NC-400-4P	0.44	2.75	1.03×10^{-5}	0.82	42.08	0.0197	0.86	3.10×10^{-3}
CoP/Co_2P@NC-400P-25P	0.42	3.06	9.45×10^{-6}	0.82	15.62	0.0538	0.83	4.33×10^{-3}
RuO_2	0.36	3.39	2.34×10^{-5}	0.77	9.53	0.0104	0.63	1.29×10^{-3}

Table S5. Comparison of HER performance of the catalysts in this work with similar catalysts reported previously.

Catalysts	Overpotential (η_{10}, mV)	Stability test duration (h) @10 mA·cm^{-2}	Ref.
CFM 0.3	241 @η_{100}	48	[3]
CoPONPCNTs/CTs	101.9	72	[4]
S-NiFe/NFF	150	-	[5]
Ni_2P@C/NF-12 h	69	48	[6]
CoP-Ni_5P_4/NF	187	12	[7]
Ni_2P/NPC/NF	58	48	[8]
NiCoP-BDC-$_4$/NF	170 @η_{50}	25	[9]
CoP-C/NiO/NF	72	10	[10]
NiCoZnP/NC	74	-	[11]
N-CoO@CoP	201 @η_{100}	24	[12]
N-Co-Ni-P	99	20	[13]
Co/CoN-NC-1	115	-	[14]
Fe-CoP NFs	112	100	[15]
Ni_2P-Ni_5P_4-CoP-C/NF	100	10	[16]
SC-FeNiCeP/NF	107	80	[17]
ZnCoNiS	134	150	[18]
MnO_x/NiCoP/NF	93	-	[19]
Co-O-Cr	87	50	[20]
FeCo-P	131	24	[21]
Fe, $CoZn_{9+9}$-NO/WC	84	12 @100 mA·cm^{-2}	[22]
MoMOF/Zif-67/MoMOF	154	-	[23]
CoP/Co_2P@NC-400-10P	127.6	100 @100 mA·cm^{-2}	This work

Table S6. Comparison of OER performance of the catalysts in this work with similar catalysts reported previously.

Catalysts	Overpotential (η_{10}, mV)	Stability test duration (h) @10 mA·cm^{-2}	Ref.
CFM0.7	220	48	[3]
CoP@NPCNTs/CTs	115.6	72	[4]
S-NiFe/NFF	174	-	[5]
Ni_2P@C/NF-12 h	205	48	[6]
CoP-Ni_5P_4/NF	223 @η_{50}	12 @50 mA·cm^{-2}	[7]
Ni_2P/NPC/NF	208	-	[8]
NiCoP-BDC-$_4$/NF	323 @η_{50}	-	[9]
CoP-C/NiO/NF	301 @η_{50}	10	[10]
NiCoZnP/NC	228	85	[11]
N-CoO@CoP	332 @η_{100}	24	[12]
Fe–Co–OOH	250	20	[13]
Co/CoN-NC-1	290	-	[14]
Fe-CoP NFs	255	100	[15]
Ni_2P-Ni_5P_4-CoP-C/NF	293	27 @50 mA·cm^{-2}	[16]
SC-FeNiCeP/NF	208	80	[17]
ZnCoNiS	146	60	[18]
MnO_x/NiCoP/NF	240	-	[19]
Co-O-Cr	203	50	[20]
FeCo-P	240	24	[21]
Fe, $CoZn_{9+9}$-NO/WC	290	28	[22]
Co/CoP@PNC-10	137	60	[24]
NiMoC-NCNTs	310	50	[25]
750+Al+P	353	-	[26]
Co-CMOF	380	-	[27]
$CoNi_{0.2}Fe_{0.05}$-Z-H-P	329	10	[28]
CoP/Co_2P@NC-400-10P	297.4	100 @100 mA·cm^{-2}	This work

Table S7. Comparison of the overall water splitting activity of the catalysts in this work with other reported bifunctional catalysts.

Catalysts	Overpotential (η_{10}, mV)	Stability test duration (h) @10 mA·cm^{-2}	Ref.
S-NiFe/NFF	1.50	80 @10, 100, 500 mA·cm^{-2}	[5]
Ni_2P@C/NF-12 h	1.55	48	[6]
CoP-Ni_5P_4/NF	1.47	50	[7]
Ni_2P/NPC/NF	1.53	48	[8]
NiCoP-BDC-$_4$/NF	1.57	38	[9]
CoP-C/NiO/NF	1.57	16	[10]
NiCoZnP/NC	1.54	45	[11]
N-CoO@CoP	1.79 @η_{100}	50 @50 mA·cm^{-2}	[12]
N-Co-Ni-P//Fe-Ni-OOH	1.71@ η_{50}	25	[13]
Co/CoN-NC-1	1.66	24	[14]
Fe-CoP NFs	1.65	100	[15]
Ni_2P-Ni_5P_4-CoP-C/NF	1.55	18	[16]
SC-FeNiCeP/NF	1.57	30	[17]
MnO_x/NiCoP/NF	1.59	200	[19]
Co-O-Cr	1.53	-	[20]
FeCo-P	1.49	24	[21]
Fe, $CoZn_{9+9}$-NO/WC	1.56	-	[22]
CoP@FeCoP/NC YSMPs	1.68	20	[29]
FeNiP/NPCS	1.71	20	[30]
$MnCo_2O_4$@Ni_2P/NF	1.63	30	[31]
$Co_{0.8}Fe_{0.2}P$	1.67	20	[32]
CoS_2/CoP@C-CNFs	1.549	112	[33]
Ni_2P-Fe_2P/NF	1.56	-	[34]
Ni_2P-Fe_2P/NF	1.68@η_{100}	48	[34]
P@pCoPc-1/Co_3O_4|CC	1.672	12	[35]
Co_3O_4-Mo_2N NFs	1.65	20	[36]

d-NiFeP/CC	1.49	50	[37]
BP(Ni_3Pd_1)	1.60	20	[38]
CoNi@N-PCNS	1.59	100@10 mA·cm^{-2} 100@100 mA·cm^{-2}	[39]
Ni-BP-3	1.605	50	[40]
CoP/Co_2P@NC-400-10P	1.58@η_{10} 1.83@η_{100}	100 @100 mA·cm^{-2}	This work

SI References

[1] J.P. Perdew, K. Burke, M. Ernzerhof, Generalized gradient approximation made simple, Physical Review Letters 77(18) (1996) 3865-3868.

[2] K. Momma, F. Izumi, VESTA 3for three-dimensional visualization of crystal, volumetric and morphology data, Journal of Applied Crystallography 44(6) (2011) 1272-1276.

[3] S. Jin, X. Liu, J. Cao, M. Wei, Y. Chen, X. Li, Q. Wu, B. Feng, M. Han, D. Jin, Z. Dong, X. Liu, H. Liu, FeCo-MOF derived Co_4S_3/Fe_3S_4/MoS_2 nanosheet arrays on iron foam for overall water splitting in alkaline water /seawater at large-current density, International Journal of Hydrogen Energy 61 (2024) 329-340.

[4] D. Kong, Q. Xu, N. Chu, H. Wang, Y.V. Lim, J. Cheng, S. Huang, T. Xu, X. Li, Y. Wang, Y. Luo, H.Y. Yang, Rational Construction of 3D Self-Supported MOF-Derived Cobalt Phosphide-Based Hollow Nanowall Arrays for Efficient Overall Water Splitting At large Current Density, Small 20(27) (2024) e2310012.

[5] L. Wu, J. Feng, Z. Zou, K. Song, C. Zeng, Formation of feathery-shaped dual-function S-doped FeNi-MOFs to achieve advanced electrocatalytic activity for OER and HER, Journal of Electroanalytical Chemistry 935 (2023) 117365.

[6] N. Chen, S. Che, H. Liu, G. Li, N. Ta, F. Jiang Chen, B. Jiang, N. Wu, Z. Li, W. Yu, F. Yang, Y. Li, Multistage interfacial engineering of 3D carbonaceous Ni_2P nanospheres/nanoflowers derived from Ni-BTC metal-organic frameworks for overall water splitting, Journal of Colloid and Interface Science 638 (2023) 582-594.

[7] J. Jiang, G. Xu, Y. Li, C. Wang, L. Zhang, Interfacial engineering of metal–organic framework derived hierarchical CoP–Ni_5P_4 nanosheet arrays for overall water splitting, Journal of Materials Chemistry A 11(4) (2023) 1801-1809.

[8] N. Chen, S. Che, H. Liu, N. Ta, G. Li, F. Chen, G. Ma, F. Yang, Y. Li, In Situ Growth of Self-Supporting MOFs-Derived Ni_2P on Hierarchical Doped Carbon for Efficient Overall Water Splitting, Catalysts 12(11) (2022) 1319.

[9] T.O. Ogundipe, L. Shen, Y. Shi, Z. Lu, Z. Wang, H. Tan, C. Yan, Nickel-cobalt phosphide terephthalic acid nano-heterojunction as excellent bifunctional electrocatalyst for overall water splitting, Electrochimica Acta 421 (2022) 140484.

[10] M. Wang, Y. Li, L. Zhai, X. Zhang, S.P. Lau, Self-supporting CoP-C nanosheet arrays derived from a metal-organic framework as synergistic catalysts for efficient water splitting, Dalton Transactions 50(47) (2021) 17549-17558.

[11] B. Chen, D. Kim, Z. Zhang, M. Lee, K. Yong, MOF-derived NiCoZnP nanoclusters anchored on hierarchical N-doped carbon nanosheets array as bifunctional electrocatalysts for overall water splitting, Chemical Engineering Journal 422(15) (2021) 130533.

[12] M.J. Lu, L. Li, D. Chen, J.Z. Li, N.I. Klyui, W. Han, MOF-derived nitrogen-doped CoO@CoP arrays as bifunctional electrocatalysts for efficient overall water splitting, Electrochimica Acta 330 (2020) 135210.

[13] P. Wang, Z. Xu, Y. Lin, L. Wan, B. Wang, Exceptional Performance of MOF-Derived N-Doped CoP and Fe-Doped CoOOH Ultrathin Nanosheets Electrocatalysts for Overall Water Splitting, ACS Sustainable Chemistry & Engineering 8(24) (2020) 8949-8957.

[14] J. Lei, Z. Li, C. Wang, H. Yao, X. Wang, J. Hu, Nanocage confined nitrogen-rich MOF-derived Co/CoN heterostructure for overall water splitting, Chemical Engineering Science 293 (2024).
[15] Y. Yuan, K. Wang, B. Zhong, D. Yu, F. Ye, J. Liu, J. Dutta, P. Zhang, MOF-Derived Iron-Cobalt Phosphide Nanoframe as Bifunctional Electrocatalysts for Overall Water Splitting, Energy & Environmental Materials 7(6) (2024) e12747.
[16] Q. Ni, Z. Zhu, Y. Wang, C. Jiang, M. Wang, X. Zhang, A pillar-layered Ni_2P-Ni_5P_4-CoP array derived from a metal-organic framework as a bifunctional catalyst for efficient overall water splitting, Dalton Transactions 53(20) (2024) 8732-8739.
[17] Q. Wang, X. Ma, W. You, P. Ma, R. Bi, S. Song, F. Chen, F. Qu, X. Wang, P. Liu, High-valence metal engineered trimetallic organic framework derived S, C co-doped FeNiCeP nanospheres for proficient self-powered overall water splitting, Chemical Engineering Journal 482 (2024) 148712.
[18] P. Li, L. Zhang, Y. Yao, T. Xie, W. Du, T. Zhao, J. Jiang, ZnCoNiS nanoflowers electrodes with rich heterointerface as efficient bifunctional electrocatalyst for overall water splitting, International Journal of Hydrogen Energy 51 (2024) 1521-1533.
[19] Z. Zhang, L. Han, K. Tao, MnO_x-decorated MOF-derived nickel–cobalt bimetallic phosphide nanosheet arrays for overall water splitting, Dalton Transactions 53(4) (2024) 1757-1765.
[20] Z. Lv, H. Zhang, C. Liu, S. Li, J. Song, J. He, Oxygen-Bridged Cobalt-Chromium Atomic Pair in MOF-Derived Cobalt Phosphide Networks as Efficient Active Sites Enabling Synergistic Electrocatalytic Water Splitting in Alkaline Media, Advanced Science 11(3) (2023) 2306678.
[21] H. Jiang, Z. Zhao, G. Li, M. Wang, P. Chen, X. Liu, X. Tu, Y. Hu, Z. Shen, Y. Wu, Hollow Spherical Heterostructured FeCo-P Catalysts Derived from MOF-74 for Efficient Overall Water Splitting, Advanced Science 11(2) (2024) e2306919.
[22] J. Xue, Z. Liu, Y. Fan, R. Wang, Y. Li, ZIF-derived Fe,Co coordinated N/O-codoped three-dimensional tungsten–carbon matrix for the performance-enhanced zinc-air flow battery and water splitting, Chemical Engineering Journal 476 (2023) 146502.
[23] S.F. Nami-Ana, S. Zeinali, Synthesis of a novel one-dimensional ternary MOF-on-MOF in form of direct and carbonization derived structure towards promising catalytic efficiency of HER, Applied Energy 350 (2023) 121755.
[24] G. Gao, D. Wei, L. Li, M. Wei, X. Chen, Y. Yu, G. Yang, G. Zhu, L. Han, J. Jia, Accordion-like Co-MOF derived heterostructured Co/CoP@PNC as highly efficient electrocatalyst for alkaline hydrogen evolution reaction, International Journal of Hydrogen Energy 51 (2024) 1333-1342.
[25] H.J. Liu, S. Zhang, W.Z. Qiao, R.Y. Fan, B. Liu, S.T. Wang, H. Hu, Y.M. Chai, B. Dong, Bimetallic metal-organic framework-derived bamboo-like N-doped carbon nanotube-encapsulated Ni-doped MoC nanoparticles for water oxidation, Journal of Colloid and Interface Science 657 (2024) 208-218.
[26] K. Sielicki, A. Matlak, X. Chen, E. Mijowska, AlP compound and P-doping for promotion of electrocatalytic activity of N-doped carbon derived from metal-organic framework, Journal of Alloys and Compounds 970 (2024) 172534.
[27] K. Sielicki, X. Chen, E. Mijowska, The role of aluminium in metal–organic frameworks derived carbon doped with cobalt in electrocatalytic oxygen evolution reaction, Materials & Design 231 (2023) 117365.
[28] M. Wang, C.L. Dong, Y.C. Huang, Y. Li, S. Shen, Electronic Structure Evolution in Tricomponent Metal Phosphides with Reduced Activation Energy for Efficient Electrocatalytic Oxygen Evolution, Small 14(35) (2018) 1801756.

[29] J. Shi, F. Qiu, W. Yuan, M. Guo, Z.-H. Lu, Nitrogen-doped carbon-decorated yolk-shell CoP@FeCoP micro-polyhedra derived from MOF for efficient overall water splitting, Chemical Engineering Journal 403 (2021) 126312.
[30] J.-T. Ren, Y.-S. Wang, L. Chen, L.-J. Gao, W.-W. Tian, Z.-Y. Yuan, Binary FeNi phosphides dispersed on N,P-doped carbon nanosheets for highly efficient overall water splitting and rechargeable Zn-air batteries, Chemical Engineering Journal 389 (2020) 124408.
[31] J. Ge, W. Zhang, J. Tu, T. Xia, S. Chen, G. Xie, Suppressed Jahn-Teller Distortion in $MnCo_2O_4$@Ni_2P Heterostructures to Promote the Overall Water Splitting, Small 16(34) (2020) e2001856.
[32] H. Wang, H. Wang, H. Wan, D. Wu, G. Chen, N. Zhang, Y. Cao, X. Liu, R. Ma, Ultrathin Nanosheet-Assembled Co–Fe Hydroxide Nanotubes: Sacrificial Template Synthesis, Topotactic Transformation, and Their Application as Electrocatalysts for Efficient Oxygen Evolution Reaction, ACS Applied Materials & Interfaces 12(41) (2020) 46578-46587.
[33] N. Liu, T. Huang, X. Liu, Z. Yu, G. Xu, L. Zhang, Synergistic interface regulation of CoS_2/CoP heterostructures supported on coal-based carbon fibers toward high-performance overall water splitting, International Journal of Hydrogen Energy 180 (2025) 151699.
[34] L. Wu, L. Yu, F. Zhang, B. McElhenny, D. Luo, A. Karim, S. Chen, Z. Ren, Heterogeneous Bimetallic Phosphide Ni_2P-Fe_2P as an Efficient Bifunctional Catalyst for Water/Seawater Splitting, Advanced Functional Materials 31(1) (2020) 2006484.
[35] Y. Kim, D. Kim, J. Lee, L.Y.S. Lee, D.K.P. Ng, Tuning the Electrochemical Properties of Polymeric Cobalt Phthalocyanines for Efficient Water Splitting, Advanced Functional Materials 31(41) (2021) 2103290.
[36] T. Wang, P. Wang, W. Zang, X. Li, D. Chen, Z. Kou, S. Mu, J. Wang, Nanoframes of Co_3O_4–Mo_2N Heterointerfaces Enable High-Performance Bifunctionality toward Both Electrocatalytic HER and OER, Advanced Functional Materials 32(7) (2022) 2107382.
[37] T. Chen, B. Li, K. Song, C. Wang, J. Ding, E. Liu, B. Chen, F. He, Defect-activated surface reconstruction: mechanism for triggering the oxygen evolution reaction activity of NiFe phosphide, Journal of Materials Chemistry A 10(42) (2022) 22750-22759.
[38] W. Zhai, Y. Chen, Y. Liu, T. Sakthivel, Y. Ma, S. Guo, Y. Qu, Z. Dai, Bimetal-Incorporated Black Phosphorene with Surface Electron Deficiency for Efficient Anti-Reconstruction Water Electrolysis, Advanced Functional Materials 33(25) (2023) 2301565.
[39] B. Yan, X. Qin, T. Chen, Z. Teng, D.K. Cho, H.W. Lim, H. Hong, Y. Piao, L. Xu, J.Y. Kim, Size and Synergy Effects of Ultrafine 2.6 nm CoNi Nanoparticles Within 3D Crisscross N-Doped Porous Carbon Nanosheets for Efficient Water Splitting, Advanced Functional Materials 34(2) (2024) 2309264.
[40] W. Zhai, Y. Chen, Y. Liu, Y. Ma, P. Vijayakumar, Y. Qin, Y. Qu, Z. Dai, Covalently Bonded Ni Sites in Black Phosphorene with Electron Redistribution for Efficient Metal-Lightweighted Water Electrolysis, Nano-Micro Letters 16(1) (2024) 115.